

¹ Masters Thesis: The Evolution of Fault Slip Surfaces with
² Cumulative Displacement

³ Kelian Dascher-Cousineau

⁴ January 9, 2017

⁵ **Abstract**

Fault slip surface roughness determines fault strength, friction and dynamic fault processes. Wear models and field observations suggest that roughness decreases with cumulative displacement. However, measurements have yet to isolate the effect of displacement from other possible controls, such as lithology or tectonic setting. We present an unprecedentedly large fault surface dataset collected in and around the San-Rafael Desert, S.E. Utah, United States. In the study area, faults accommodated regional extension at shallow 1 to 3 km depth and are hosted in the massive, well sorted, high porosity Navajo and Entrada sandstones. Existing detailed stratigraphic throw profile provide a maximum constraint for displacement. Where cross-sectional exposure is good, we measure exact displacement imparted on slip surfaces using offset in marker horizons. Thereby, we isolate for the effect of displacement during the embryonic stages of faulting (0 to 60 m in displacement). Our field observations indicate a clear compositional and morphological progression from isolated joints or deformation bands towards smooth, continuous and mirror-like fault slip surfaces with increasing displacement. To quantify these observations, slip surfaces were scanned with a white light interferometer, a laser scanner and a ground based Lidar. Together these instruments resolve more than eight decades of spatial bandwidth (from less than μm 's to m's in scale). Preliminary results indicate that roughness decreases with displacement according to a power law. Roughness measurement associated with only maximum constraints on displacements corroborate this result—for a given displacement, minimum roughness is bounded by the later smoothing trend. In addition, we find that the maximum roughness is fixed—bounded a by a primordial roughness corresponding to that of joints surfaces and deformation band edges. Our results build towards a coherent model of fault wear robust to ambiguities associated to displacement estimates, spatial scaling and geological context.

³⁰ *Will have to include relationship to white light data, modelling results/interp*

³¹ **Contribution of Authors**

³² **1 Introduction**

³³ Would closely follow my project proposal:

³⁴ **1.1 Motivation**

³⁵ Faults are a characteristic feature of the Earth's brittle crust. Fluid flow, seismicity and crustal
³⁶ mineralization are just few systems upon which faults act as major controls (Sibson, 1977). In
³⁷ spite of their importance, some aspects of faults and their underlying processes remain poorly

understood. How strong is a fault? How do faults mature? Are small faults mechanically different to large faults? Fault geometry has been shown to be a key parameter controlling the mechanical behavior and evolution of faults (e.g. Lay et al., 1982; Aki, 1984; Power et al. 1988; Chester and Chester, 2000), but these questions are not yet fully answered.

Slip on a fault occurs on discrete slip surfaces in fault zones (Davatzes and Aydin, 2005). These surfaces are not planar; they are rough. Roughness is observable at all scales (Scholtz and Aviles, 1986; Candela et al., 2012). Slickenlines, corrugations, mullions and jogs are all surface features that can be seen at different length scales (Sagy and Brodsky, 2009). Field studies have found common characteristics in the topography of fault surfaces. These can be summarized as follows: 1) Fault surfaces appear to be well defined by large fractal domains, wherein 2) faults are smoother at larger length scales (Scholtz and Aviles, 1986; Candela et al., 2012), 3) rougher in the slip perpendicular direction than in the slip parallel direction (Lee and Bruhn, 19960, and 4) slip surfaces are smoother with cumulative displacement (Sagy et al., 2007). Fault roughness has been demonstrated to be critical in determining the strength (Chester and Chester, 2000, Brodsky et al., 2016), triggering (Parsons, 2008), dynamic properties (Candela et al., 2011; Dunham et al., 2011), spatial distribution (Parson, 2008) and failure recurrence of faults (Stirling et al., 1996). It is increasingly evident that roughness is a fingerprint of fundamental features of the faulting process (Brodsky et al., 2016). In accordance, incorporating more complex sources geometries has become a more frequent practice in dynamic earthquake rupture modelling (Shi and Day, 2013; Dunham et al., 2011).

Changes in roughness, as determined by cumulative displacement (Sagy et al, 2007; Brodsky et al, 2011), imply faults mature. Fundamental differences between immature and mature fault have far-reaching implications. Fixed source parameter scaling of earthquakes is a pillar of earthquake seismology. However, analysis of seismic signals of immature faults vs. mature faults suggest that scaling is sensitive to cumulative displacement. This observation leads to an interpretation of fundamental differences in earthquake populations. Specifically fault maturation would undermine the applicability of a constant magnitude scaling. Evolving mechanical properties such as fault friction and static strength—both associated to fault roughness—would imply that immature and mature faults belong to distinct populations with distinct scaling. (Harrington and Brodsky, 2011)

While there has been significant progress in understanding the role of roughness in the faulting process, how and why fault surfaces change is still unclear (e.g. Candela et al., 2011; Dunham et al., 2011; Brodsky et al., 2016). Sagy et al. (2007) noted a systematic decrease in roughness of ‘mature’, large displacement faults compared to ‘immature’ faults with low displacements. Similar results have since been observed along reactivated joints, in laboratory experiments (Davidesko et al., 2014), and in compilations of fault roughness analysis (Brodsky et al., 2011; Candela et al., 2012). These studies all attribute the decrease in roughness to wear at the fault interface. However, these data show only weak correlations between fault roughness and cumulative displacement. Indeed, relating roughness and cumulative displacement is not trivial. Fault surfaces in exhumed faults are rarely well preserved. Furthermore, obtaining well-constrained displacement estimates is contingent on the presence of precise and accurate kinematic indicators. Combining observations over a broad range of displacements is challenging. Consequently, it is unclear whether trends observed in compilations of roughness measurements from multiple faults are directly attributable to displacement or a combination other geological factors. For instance, while comparing fault surfaces from geologically diverse datasets, variations in lithology, faulting mechanism, temperature and depth may all be introducing further systematic variations.

Additionally, the evolution of roughness represents a novel insight into the architecture of a fault zone. The geometry of the fault surface modulates the architecture of the whole fault zone (Mitchell and Faulkner, 2009). Changes in roughness require interaction between the slip

surfaces and its direct surrounding (fault core), resulting in the formation of fault rock (Power and Tullis, 1988). In addition to earthquake mechanics, the architecture of a fault zone, and its corresponding permeability structure, is very important for hydrocarbon exploration (Shipton and Cowie, 2003). However, because the change in roughness by wear is poorly understood, the equivalent production of wear material, the fault rock, is also poorly understood. Fault rock thickness growth with displacement is documented (Sholtz, 1987), but variability is such that even order of magnitude estimates of thickness for a given displacement are unavailable.

The objective of this project is to identify how and why fault surfaces change. In line with previous studies, I hypothesize that wear is a dominant mechanism in the evolution of fault surfaces with cumulative displacement. I will measure the surface roughness of natural fault surfaces with varying displacements to confirm and better quantify the role of cumulative displacement on fault roughness. This study will be broadly composed of the following three components: 1) data collection, 2) data processing and analysis and 3) interpretation of the results. Field work in Southern Utah will be conducted with the specific intent of collecting scans of pristine fault surfaces with terrestrial laser scanners and hand-samples for laboratory high resolution scans. The roughness of the surfaces will then be quantified and related to corresponding displacement. A robust quantitative correlation between roughness and cumulative displacement will enable parameterized interpretation and modelling of the mechanics of fault wear. Based on my results, I will explore the mechanical implications of a changing fault surface as coupled to the fault zone. In this proposal, I first present the geological background and important concepts. I then follow by outlining the projected scientific method, data analysis and interpretation. I conclude with a time line for the completion of my thesis in a timely two year period.

1.2 Fault Roughness

The deviation from planarity formally defines roughness (Brown and Scholz, 1985). Pioneering studies used contact profilometers to measure the roughness of fault surfaces (Scholz and Aviles, 1986; Power and Tullis, 1991. Combined with surface profiles of large scale continental faults, faults were found to have a remarkably broad fractal band ranging over 10 orders of magnitude—from 10^{-5} to $10^5 m$ (Scholz and Aviles, 1986). Over these length scales, fractal scaling is said to be statistically self-affine. A statistically self-affine profile along x with heights $h(x)$, is invariant under the affine transformation:

$$\begin{cases} x \rightarrow \lambda x \\ h \rightarrow \mu h \end{cases} \quad (1)$$

This relation therefore implies an exponential relation between the scaling, λ (along x), and μ (along h) such that:

$$\mu = \lambda^\varsigma \quad (2)$$

Where ς is a constant named the Hurst exponent. Note that self-similarity, is an instance of self-affinity where the Hurst exponent is 1 (Schmittbulh et al., 1993). Developments in laser scanner technology over the past decade, particularly terrestrial laser scanners, allowed surfaces to be characterized by calculating the Hurst exponent from thousands of cross sectional profiles through a fault surface (e.g. Candela et al., 2012). Studies of natural mode I crack surfaces have observed self-affinity with a Hurst exponent of ~ 0.8 at all scales of observation (Scholtz, 1985). Shear, or mode II cracks (i.e. faults) are different. They are anisotropic—the Hurst exponent parallel to shear (~ 0.6) is smaller than that in the shear-perpendicular direction (~ 0.8) (Lee and Bruhn, 1996).

Another parameter is required to fully describe surface roughness. While the Hurst exponent describes the scaling behavior of the roughness it does not define the magnitude of the roughness. The pre-factor defines the amplitude of the scaling law (Candela et al., 2009). The pre-factor is subject to significant variation. Overall, observations show that fault surfaces have distinctly smoother profiles along slip direction than perpendicular to slip (Lee and Bruhn, 1996). Many methods exist to quantify roughness scaling, possibly most intuitive of which is the Root Mean Squared (*RMS*) as a function of scale. For a profile of length L with a point spacing of Δx with deviation h from the best fit line, the *RMS* for a given scale s is defined as follows:

$$RMS(s) = \sqrt{\frac{\Delta x}{L} \sum_{i=1}^{L/\Delta x} h_i^2} \quad (3)$$

The *RMS* roughness of a fault or fracture exhibits power-law scaling with segment length. A self-affine profile should therefore plot as a straight line on a log-log plot of the *RMS* as a function of the segment length with a slope equivalent to the Hurst exponent. (Schmittbuhl et al., 1993) The power spectrum of a surface profile has been shown to yield more robust roughness metrics (Schmittbuhl et al., 1993; Candela et al., 2009). For a set of discretely sampled points, the power spectrum of a profiles is the result of a Fast Fourier Transform (FFT). The spectrum defines the surface profile as superposition of sinusoidal profiles. In the frequency domain, rougher profiles will have correspondingly higher amplitudes, or power. The power spectrum, $P(k)$, of a self-affine profile (again in log-log space) defines a line as follows:

$$P(k) = Ck^{(-1-2\zeta)} \quad (4)$$

Where k is the frequency and C is the pre-factor (Candela et al., 2009).

1.3 Wear

1.4 The evolution of slip surfaces with displacement

talk about deformation in sandstones, e.g. aydin, fossen etc.

In this project, I hope to address how slip surfaces change. Many processes could cause the slip surface to change. In fact, the cause of change to the slip surface is not uniquely recorded by the roughness. Fundamentally, a fault surface can only change according to the following mechanisms:

Addition of material

Redefinition of the slip surface by fracture

Removal of material

I have hypothesized that the change in surface roughness is the result of wear—an instance of removal of material. As fault blocks slide past each other, frictional wear is an inevitable process. Layers of comminuted fault rock are direct evidence of this process (Power and Tuillis 1988). Wear is the subject of a vast field of research, particularly in engineering and tribology due to interest in lubricating and manufacturing machine parts for longevity (Meng and Ludema, 1995). Here, I outline only basic wear mechanics (i.e. Archard, 1953). Wear is formally defined as frictionally induced volume removal from surfaces in sliding contact. The wear rate, the amount of wear per unit distance is broadly related to the real area of contact and loading. When two surfaces are put in direct contact, the real area of contact is much smaller

than the nominal surface areas because the load is supported at microscopic protrusions from a surface, called asperities. Remote loading normal to the surface causes local stresses and associated deformations at contact points. Note that as the load is increased, deformation of large asperities causes new asperities to come in contact. In its simplest form, wear rate defined as:

$$W \propto \frac{P}{a} \quad (5)$$

Where W is the wear rate, P is the remote load and a is a mean measure of the dimensions of the asperities in contact during sliding. The relation has been shown to be reasonably robust in experimentation for most materials. In further detail, the size, distribution and duration of contact areas, as well as the shape of the worn particles, control the general behavior of wear. Note that material properties are implicitly buried in a probability factor—the probability of a collision of asperities to lead to removal of material (Archard, 1953). If and how wear affect the geometry of a fault slip surface remains unclear. Both field and laboratory experiment show that wear is scale dependent, such that asperities are worn down at different rates according to their typical dimensions. Asperities at longer characteristic wavelengths and larger amplitudes wear down faster, on average, than those with small wave lengths and small amplitudes. These observations correspond to both a downward translation and clockwise rotation of the self-affine scaling in the power spectrum. The exact mechanism causing this behavior is unclear. Davidesko et al., 2014 suggest that dilation during displacement on a fault ‘shelters’ smaller, shorter wavelength, asperities and therefore wears down large, long wavelength asperities. In this study, I hope to be able to relate changes in the slip surface geometry to wear processes. Specifically, empirically identifying and determining the rate of wear as expressed in the slip surface would be of particular interest. A potential caveat to the simple wear models (i.e. Archard, 1953) is the sensitivity of fault rock to sliding velocity and the presence of lubricant (e.g. pseudotachylyte, amorphous silica gel and gouge). Moreover, the stresses imparted by a propagating fault rupture front are mechanically distinct from those related to rubbing surfaces. Such a distinction may also drastically alter the relation between wear material and the slip surface (Sibson, 1977). Since Archard (1953), models of wear tend to diverge in their results, assumptions and by association, their applicability (Meng and Ludema, 1995). For the purpose of this study, the fractal nature of fault surfaces is important to reconcile with a model of wear. What is the scaling behavior of wear? Fractal surfaces are difficult to integrate into the pre-existing framework of wear processes. Specifically, defining the real area of contact, corresponding deformation and, by association, the scale dependence of wear is non-trivial (e.g. Persson, 2001; Jackson and Streator, 2006).

1.5 Objectives of this study

2 Geology

maybe put as a separate section (like 2)

Field work will be conducted in the San-Rafael Desert, Utah (see figure 1). The San Rafael Desert hosts a sequence of gently dipping marine and sub-areal sedimentary rocks deposited from the Pennsylvanian to the Jurassic (see Figure 2). The San Rafael Desert is part of the San Rafael Swell, a monocline that formed when these sediments were uplifted as a passive drape fold above a reactivated basement reverse fault during the Late Cretaceous Laramide Orogeny (Kelly, 1955; Vrolijk et al., 2005). The swell is part of the broader Colorado Plateau (Kelly, 1955). Networks of joints and normal faults associated to further Laramide activity cross-cut sedimentary sequence accommodating North-South extension (Aydin and Johnson,

1978; Vrolijk et al., 2005). Specifically, within the San Rafael Swell we have selected the following field locations: 1) the Chimney Rock Fault Array, 2) the Big Hole fault and 3) a network of deformation bands in the Entrada formation near Goblin Valley State Park. Advantages of these field locations are manifold. First, the nearly pure quartzite lithology, extensional tectonic regime, depth (2-4 km or 40-80 MPa), temperature (estimates range from 45-90 °C) of activity, and faulting mechanism are all relatively consistent (Vrolijk et al., 2005). Consistency in these parameters is key to isolating the effect of displacement on the fault roughness. Moreover, both field locations exhibit well preserved fault surfaces that are exposed and accessible (see Figure 3). The Chimney Rock fault array is an orthorhombic set of faults that crops out at the northern end of the San Rafael Swell (Krantz, 1989, Davatzes et al., 2003). Two pairs of oppositely dipping normal faults crop out at the surface with preserved fault scarps. WNW-striking faults are interpreted to have formed by shear reactivation of joints, whereas ENE-striking faults initially formed from deformation bands (Davatzes, 2003). Exposure is very good, faults are abundant and have well preserved fault surfaces (Vrolijk et al., 2005). The Chimney fault array has studied to better understand of fault geometry (Shipton and Cowie, 2001; Shipton and Cowie, 2003), permeability (Shipton et al., 2002) and kinematics (Krantz, 1986; Krantz, 1989; Maerten et al., 2001; Davatzes et al., 2003) . As a result, detailed maps of the fault array have been produced (e.g. Maerten et al., 2001) . In addition, by using measurements of the separation between footwall and hanging wall cutoffs of sedimentary horizons, entire displacement profiles have been measured for faults with a wide range of displacements (Cowie and Shipton, 1998; Maerten et al., 2001; Shipton and Cowie 2001; Shipton and Cowie, 2003). The Big Hole fault is located just to the South-East of the Chimney Rock Fault Array. While not explicitly part of the fault array, the Big Hole fault shares a nearly identical geological setting. The Big Hole fault has been extensively studied in detail as an analog to hydrocarbon reservoir-scale faults. Displacements on the exposed fault range from 8 m to 39 m. (Shipton and Cowie, 2001; Shipton and Cowie, 2003) Large networks of deformation band faults outcrop near Goblin Valley State Park on the southeastern margin of the San Rafael Swell (Aydin and Johnson, 1978). Deformation bands are the result of concentrated shear deformation on narrow centimeter thick bands (Aydin and Johnson, 1978; Davatzes et al., 2003). Collapsing pore space accommodates this deformation. Deformation bands are interpreted as the embryonic stages of fault development (Fossen and Hesthammer, 1998; Fossen et al., 2007). Because deformation bands dramatically alter the local permeability structure, Goblin Valley has been extensively studied in light of fault nucleation and the implications for hydrocarbon circulation (e.g. Fossen et al., 2005; Tobari and Fossen 2009). At Goblin valley, arrays of deformation bands anastomose—outcropping as centimeter- to meter-sized slabs. These are often bounded by discrete slip surfaces with well-preserved striations — i.e. roughness (Aydin and Johnson, 1978). Offsets in sedimentary beds have allowed previous studies to obtain detailed displacement measurements (e.g. Schultz and Fossen 2002). Together, these field locations offer the chance to survey well-preserved fault surfaces that have hosted displacements from embryonic stages to 30 m of displacement. Moreover, novel to this study, we will be able to survey multiple expressions of a single fault's surface with various displacements according the displacement profile of the fault.

3 Method

3.1 Data Collection

In this study, I aim to quantitatively describe the evolution of fault slip surfaces. In addition, I will address the question of how fault slip surfaces evolve and the implications thereof. Key elements for the success of this study are the quality of the displacement measurements and

the large number of accurate surface scans. Objectives for the field work and data acquisitions thus reflect these standards. To prepare for the coming field season, I am making efforts to obtain raw data of previously measured displacement profiles. These profiles should provide the necessary data to constrain displacement at outcrops with good fault exposure. I also hope to have good base maps ready to work with in the field for the Chimney Rock Array, Big hole and Goblin Valley field areas. To measure surface roughness, a flexible array of instruments is necessary (Brown and Scholtz, 1985; Candela et al., 2012). Scans will be obtained with three instruments, which have complimentary scales of observation. At scales ranging from meters down to millimetres, a light detection and ranging instrument (i.e. LiDAR) is the ideal instrument from high resolution surface scans. At intermediate scales ranging from centimetres down to hundreds of microns, a 3D laser scanner will potentially be brought in the field. A NextEngine 3D laser scanner is available for use at McGill. The NextEngine laser scanner offer accuracy down to 100 microns with resolution up to 268,000 points per square inch. Finally, at scales ranging from millimeters down to sub-micron, a white light interferometer will be used to scan hand samples collected in the field. This instrument is available at the McGill Nanotools Microfab labs. Combined, these instruments offer accurate and precise three dimensional sampling of fault surfaces at over nine decades of length scale. All the scans that will be collected will be associated with a corresponding displacement on the fault surface. These will either be collected by direct observation of sedimentary offset (where easily measurable) and/or from pre-existing displacement profile. In parallel to the analysis of the surface roughness using surface scans, the nature, volume and distribution of wear product on the fault will be recorded in the field. Hand samples were collected for surface and petrographic analysis. Together, all these measurements and observations should provide the necessary data to robustly explain and quantify the process through which faults mature.

3.1.1 Field procedure

the instruments could be in a table

3.1.2 Lidar

3.1.3 Laser Scanner

3.1.4 White light

3.1.5 Displacement estimates

3.2 Scan data Processing

In this section, I present the work flow for processing scan data. We use spatial statistic to characterize and infer processes active on faults—specifically on the slip surface. To do so the following work flow is implemented *MatLab*:

1. Preprocessing
 - (a) manual inspection for coarsest defects
 - (b) Import *.xyz* data into *Matlab*
 - (c) Very coarse Height field filter
 - (d) Flatten points
 - (e) Grid data
 - (f) Orient grid along slip direction (using power spectral analysis)

- 300 (g) Remove defects
- 301 i. Remove outliers in the height field
- 302 ii. Fractal model filter
- 303 iii. Remove abnormally flat (interpolated) sections

304 2. Processing

- 305 (a) Statistical analysis
- 306 i. Scale dependent *RMS*
- 307 ii. Scale dependent skewness
- 308 iii. Scale dependent kurtosis
- 309 iv. Scale dependent asymmetry
- 310 (b) Spectral Analysis
- 311 i. Fast Fourier Transform (FFT)
- 312 ii. Lomb-Scargle Periodogram

313 *make into figure, include bypasses and other recent additions*

314 3.3 Surface Pre-processing

315 Before conducting a statistical analysis scan data must be pre-processed into a workable format.

316 Scan data has the form of point cloud data - a series of points with coordinates x , y and z .

317 Scans obtained in this study typically yielded on the order of 10^6 to 10^7 points. In raw form, the

318 point clouds are randomly oriented, noisy and still contain artefacts of defects on the scanned

319 surface. All these features must be removed. The process of manual removal is labour intensive

320 and infeasible for a data set of the scope presented in this study. I rather opt to automate this

321 process. Only very large defects (defects that may substantially effect the quality of finding a

322 true mean plane) are manually removed.

323 3.3.1 Point Cloud orientation

324 In order to yield proper spatial statistics, the surface must both be flattened and aligned along

325 slip. Linear trends in the data induce unwanted signal in the scan data and effect the quality

326 of later interpolation onto a grid. Thus, x , y , z data is rotated using around the axis \mathbf{u} as

327 determined by the normalized cross product between the surface normal \mathbf{n} and a vector normal

328 to a flat surface ($\mathbf{n}_2 = [001]$):

$$\mathbf{u} = \mathbf{n} \times \mathbf{n}_2 / |\mathbf{n} \times \mathbf{n}_2|$$

329 with the rotation,

$$R = \cos \theta \mathbf{I} + \sin \theta [\mathbf{u}]_x + (1 - \cos \theta) \mathbf{u} \otimes \mathbf{u},$$

330 where $[\mathbf{u}]_x$ is the cross product matrix of \mathbf{u} and \otimes is the tensor product and I is the identity

331 matrix.

332 At bandwidths larger than the microscopic scale, fault surfaces are anisotropic. The anisotropy

333 is associated to the direction of slip. The 'smoothest' direction is slip parallel; the 'rough-

334 ness' direction is perpendicular to slip. In this study, we narrow down our analysis to these two

335 most extreme cases. As such the fault scan is rotated to be aligned with the direction of slip.

336 The direction of slip is detected to within a degree by determining the smoothest direction by

337 spectral analysis. This process is streamlined by decimating raw data iterating steps of regrid-
338 ding, rotating and spectral analysis. For the purpose of this analysis, roughness is parameterized
339 as the integral of the log-weighted power spectrum over the entire bandwidth of the sample
340 surface. The angle associated to the minimum in roughness is then identified as the direction
341 of slip and, sequentially, used to rotate the entire flattened data cloud. The data is then
342 interpolated onto a grid using a linear interpolation algorithm.

343 **3.3.2 Surface Defect Removal**

344 INCLUDE HISTOGRAMS FOR EACH FILTER

345 Defects are filtered out of the original surface using multiple thresholding methods. The
346 basis of these methods all revolve around identifying clear points or segments that are statistical
347 outliers to the distribution characterizing the entire surface—abnormal points.

348 The most aggressive filter implemented is the fractal model outlier. The filter removes entire
349 segments with abnormally high variance in the height field for the given scale of observation.
350 For this implementation, I iterate over 10 scales. The scales are selected using a log spacing up
351 to the size of the entire surface. The threshold for segment removal is chosen to be four standard
352 deviations from the mean. Note that the filter should not be associated to a systematic bias.
353 Segment removal is symmetric. As a result, given a truly stationary fault surfaces (as assumed
354 in the subsequent analysis) the removal of extreme values should not systematically affect the
355 data. Outlier associated with a truly distinct genetic mechanism (in this case cracks and other
356 defects) *will* be removed.

357 Abnormally flat sections arise as the result of triangular interpolation of sparse points.
358 Typically, interpolation on the edge on a non-convex set of points has this effect. These artefacts
359 are removed by removing abnormally low curvatures in the log-transformed absolute value
360 curvature field. The filter rejects point with curvatures less than 10^{-25} . These values are
361 unrealistically small and can only be associated to the linear interpolation scheme.

362 Finally, all scans are inspected to make sure that the pre-processing was successful. The
363 script fails to properly process scans that are excessively populated with surface defects. These
364 scans were manually cleaned and oriented before re-processing them. Manual changes were
365 executed in *CloudCompare*.

366 **3.4 Statistical Analysis**

367 **3.4.1 Spectral Analysis**

368 **3.4.2 More Spatial Statistics**

369 INCLUDE A FIGURE WITH: ORIGINAL SURFACE, AUTOMATICALLY PROCESSED
370 GRID, MANUALLY PROCESSED GRID AND CORRESPONDING POWER SPECTRA.

371 **4 Results**

372 **4.1 Observations**

373 *include microstructure*

374 **4.1.1 Slip Surfaces**

375 The slip surface is an interface that localizes shear displacement. Fresh slip surfaces in the
376 sandstones in this study have a vitreous finish. Striations, grooves and mullions mark the

Location	Lithology	Description	Displacement Constraints
Chimney Rock Fault Array	Contact between the Navajo Sandstone and the base of the Carmel Unit	Orthorombic set of normal faults with preserved faults scarps of Navajo Sandstone	Displacement profiled of stratigraphic throw constrained by offset on a Carmel Limestone Marker Horizon by Maerten et al., 2000.
Big Hole Fault	Navajo Sandstone	On single large normal fault structure partitioning displacement on two major strands traceable for kilometers through a river wash with scarp exposure, strike parallel and strike perpendicular cross-sectional exposure	Displacement constrained using the top Erosionally competent horizon at the top of the Navajo by Shipton and Cowie, 2003 and directly where possible.
Iron Wash	Good exposure in Navajo Sandstone	Extensive network of normal and strike-slip cross-cutting faults. Very little scarp exposure but good three dimensional cross-sectional exposure which can reveal pristine slip surfaces with a bit of hammer work	Displacement mostly constrained by direct measurement of offset in the Upper Navajo horizon.
Molly's Castle	Entrada Sandstone	East-West striking network of normal faults and ubiquitous deformation bands. Well preserved slip surfaces broadly associated to a single slip surface structure intermittently bounding and crosscutting a thick (30 cm cluster of deformation bands	Displacement constraints available in places from mapping by Aydin (1978) and directly measured using various marker horizons within the Entrada Sandstone (e.g. laminae, cross-bedding unconformities, and thick red sandstone horizons depending on scale)

Table 1: Table caption



Figure 1: Left: Example of at least two distinct polished slip surfaces on the same fault structure. Right: Example of concentric pattern on cross-sectional view a fault

377 direction of slip. In Cross-section slip surfaces are relatively planar, continuous and have a
 378 milky white color. Slip perpendicular profiles are notably more sinuous than in the slip parallel
 379 direction. Fault rock sometimes bounds slip surfaces—often asymmetrically. The lithology of
 380 the fault rocks is varied. Breccia, cataclasite and gouge where all observed. Preservations
 381 of slip surfaces only occurs in the Navajo and Entrada Sandstones. In fact, in spite of good
 382 exposures of the Navajo-Carmel contact at prospecting pits at the Chimney Rock fault array
 383 and careful inspection of the slip zone, the "mirror" image of excavated slip surfaces on the
 384 Navajo Sandstone where not polished. It is unclear whether this indicates that the Carmel units
 385 is more susceptible to erosion/alteration or if the polish finish is only a feature of the quartzite
 386 sandstones. Interestingly, on North fault (a fault within the Chimney Rock fault array), the
 387 slip surfaces directly on the interface between the two units with large displacement (likely
 388 around 50 m based on rake orientation and stratigraphic throw) has a distinct deep grey color
 389 with a pristine vitreous finish. It is interesting to contemplate the possibility for lithological
 390 mixing of a gouge-like wear product producing the "base" for the slip surface material.

393 The existing model for fault evolutions prescribes a *principle slip surface* (PSS). The PSS is
 394 described as a surface that can accommodate a mechanistically limitless amount of displacement
 395 on the fault. In accordance, in exhumed faults we expect the PSS to overwhelmingly accommo-
 396 date displacement on the fault zone. However, in the field we often observe not one, but many
 397 slip surfaces. Partitioning of total displacement across multiple slip surfaces is thereby ambigu-
 398 ous. The existence of two large scale structures, both accommodating meters of displacement
 399 at big hole is a macroscopic example of this mechanism. In accordance, Shipton and Cowie,
 400 2003 report large uncertainty (many meters) on the partitioning of slip on the two strands (we
 401 have greatly reduced this uncertainty by careful inspection of stratigraphic offset. At smaller
 402 scales of observation (on the order of centimeters), many scarp outcrops show indications of
 403 many slip surfaces cross-cutting each-other. For examples, samples collected are bounded on
 404 both sides by vitreous slip surfaces. I did observe a certain concentric pattern in cross-sectional
 405 exposures (see figure 1). I interpret the concentric pattern to indicate a smoothing process by
 406 truncation of asperities. As such "older" slip surfaces would on the outside and, concentrically,
 407 "younger", more recently active surfaces would be on the inside.

408 It is unclear what controls the onset of stable slip surfaces within deformation band clusters

409 In some cases a clear PSS is unambiguously identifiable. For instance, where cross-sectional
 410 exposure reveals a single fault slip surface, we must conclude that the entire displacement is
 411 accommodated in a single slip surfaces (see figure 2. Based on such instance we characteristically
 412 further the definition of the PSS as follows:

- 413 • The PSS is an interface between two displaced fault blocks. As such juxtaposition of two
 414 distinct rock types (e.g. distinct stratigraphic horizons and/or fault rock) by faulting is

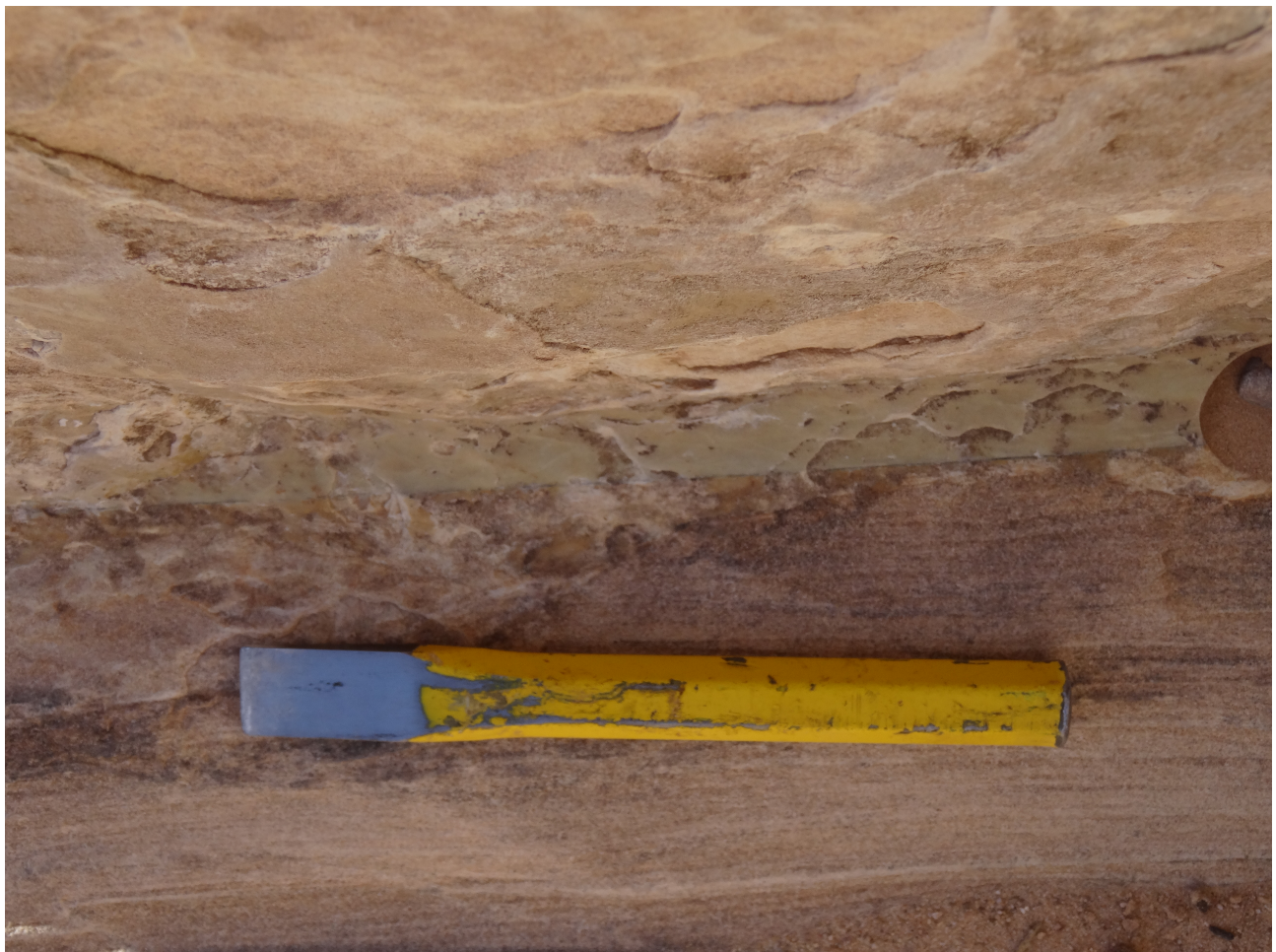


Figure 2: Example of a slip surface interpreted as a principle slip surface with around 20 meters of displacement at Big Hole Fault

415 an unambiguous

- 416 • *The PSS has a distinctly sharp, continuous, relatively planar morphology in cross section.*
417 A certain panarity must exist to prevent substantial geometric mismatch.
- 418 • *In line with the implicit definition of a fault, the PSS is nearly cohesionless.* Locations
419 identified to be expose section of a PSS inevitably cracked open when sampling across the
420 slip surface—the slip surfaces had no cohesion. Cohesion is typically thought to reinstate
421 by precipitation and healing. We did not observe ubiquitous healing at the locations in
422 this study.
- 423 • *The PSS with have a vitreous finish in quartzite sandstones*
- 424 • *The PSS is in the center of a damage zone.* Damage is an inevitable consequence of
425 displacement and the accompanying mismatch that accumulates. Damage at the field
426 locations in this study is expressed as comminution (*e.g.* cataclasite and gouge), frag-
427 mentation (*e.g.* breccia, splay joints) and shear deformation (specifically deformation
428 bands).

429 More characteristic features may come to light when analysing samples in thin-section.

430 4.1.2 Fault Rock

431 In this study we refer to *fault rock* as rock altered either mechanically or chemically by the
432 influence of the fault. At all field locations we observe diverse fault rock lithologies, ranging
433 from finegrained cataclasites to massive bodies of breccias (up to meters of thickness).

434 We suspect some fault rock associations exists. For instance, Davatzes et al., 2002 reports of
435 a systematic association between the lithology and the orientation of the fault set. Namely, the
436 orthorhombic fault set striking WNW has systematic association with fragmentation, ubiq-
437 uitous fault rock; whereas the ENE fault set rather has slip surfaces cutting through deformation
438 band clusters (see figure ??). This relations may the result of contrasting genetic mechanism.
439 The WNW set is the result of the reactivation of regional joints. In contrast the ENE fault set
440 is the the result of clustering and anastamosing deformation bands acting as a catalysing agent
441 to the formation of a faults.

442 4.1.3 Deformation Bands

443 Deformations bands where a nearly ubiquitous feature of all fault structure in the the high
444 porosity sandstones featured in this study. Deformation bands accommodate small amounts
445 of deformation by the run-away collapse of grains in sub planar sheets—or bands (as seen in
446 cross section). Around fault structures, deformation bands most often accomodate small (up
447 to a few centimetres) of shear offset across thin (up to a centimetre thick) bands. Unlike slip
448 surfaces these do not reduce the relative cohesion of the rock. It was not possible to crack them
449 open. In zones of intense shear, deformation band clusters occur. The clusters are networks of
450 anastamozing deformation bands.

451 By the reduction of grain size and compaction, deformation bands are relatively stronger
452 than the host sandstone. Correspondingly, deformation bands preferential resist erosion and
453 outcrop as slabs up to meters in sizes (especially in the Entrada Sandstone). The edge of
454 the slabs is coated with a host sand grains. In cross section, deformation bands have a milky
455 white colour and have a sinuous trace—moreso than than slip surfaces. Albeit, it is sometimes
456 difficult to differentiate slip surfaces from deformation bands in cross-section. The edge of
457 deformation band clusters appear to have a distinct "lumpy" morphology. Moreover, there is
458 a clear directional asymmetry (see figure 3)

459 Ultimately, given sufficiently intense deformation, it is thought that faults develop on one of
460 the edges of the cluster. Presumably, the mechanically stronger properties of the deformation
461 bands lead the concentration of stress around the clusters. Observations from this study do
462 not necessarily agree with this paradigm. Deformation bands active after the onset of a stable
463 slip surface *have* been observed at Big Hole (Shipton and Cowie, 2003). These are presented
464 as fault related damage. Onset of late deformation bands may reconcile our observations with
465 the existing paradigm for fault development in high porosity sandstones. We intend to explore
466 the surface roughness of the edge of deformation band clusters. In a sense, these surfaces could
467 represent a 'primordial roughness'.

468 At some locations, take for instance the Blueberry Fault in the Chimney Rock Fault Ar-
469 ray, deformations bands seems to be the overwhelming mechanism to accommodate off-fault
470 damage. When considering issues of fault mismatch related to roughness and consecutive dis-
471 placement, deformation bands may be an effective mechanism to accommodate inelastic fault
472 perpendicular deformation.



Figure 3: Left: Example of the edge of a deformation bands cluster at Molly's Castle. Note the "lumpy" morphology and an clear vertical directional asymmetry. Right: Cross-sectional view of a deformation band cluster with tens of centimetres of shear offset. It is unclear whether there is a through going slip surface localizing displacement. It is, however, definitely not on the edge of the cluster.

473 4.2 Roughness measurements

474 figures to include:

- 475 • all spectra
476 • increasing anisotropy (two surfaces) - polar plot

477 4.2.1 Lidar

478 qualitative illustration of maturity

479 **4.2.2 Laser scanner**

480 **4.2.3 White light**

481 **4.2.4 Interpretation of field observations and roughness measurements**

482 **5 Model**

483 **5.1 Modelling Objectives**

484 **5.2 Model Outline**

485 In this study, we utilize work minimization numerical modelling to capture the growth
486 of fault damage and the effect of rough asperities. The models are built off of fric2d
487 and growth by optimization of work (GROW) developed by Michele Cooke and Jessica
488 McBeck.

489 **5.2.1 GROW**

490 Growth by optimization of work predicts fracture propagation paths. It does so by mini-
491 mizing the external work on the system. The model theoretically allows for the simulta-
492 neous growth of multiple fractures and

493 The general algorithm uses a boundary element method to describe the fractures–linear
494 dislocation elements that discretize the entire length of the fault. As a crack grows,
495 dislocation elements are added radially to the tip of the crack so as to minimize the
496 external work on the system normalized by the crack area ($W_{ext}/\Delta A$). External work is
497 further defined as:

$$W_{ext} = \oint (\tau u_s + \sigma_n u_n) dB \quad (6)$$

498 **5.3 Model Results**

499 **6 Discussion**

500 **6.0.1 Tying the model together with roughness measurements and model**

501 wear rate (character), tying together model with

502 **7 conclusion**

503 **7.1 future work**

504 **8 Appendix**

505 **8.1 Surface Processing scripts**

506 Or possibly a link to a git repository...

507 8.2 User manual for script

508 This manual should serve as both a basic guide to the logic and usage of the *surface
509 processing package*.

510 The master function of the package is *surfaceprocessing*. This function effectively deal
511 with the inputs and direct computations towards the necessary functions. Outputs of
512 the function are a .mat workspace file for each input data file. The workspace includes
513 a structure (called *parameters*) with the raw surface analysis outputs, the point spacing,
514 the decimation factor (if any), the file name and the date of the analysis. The workspace
515 also includes the grid form of the original inputed surface (called *surface*), and the pre-
516 processed copy that was used for the subsequent analysis (called *zGrid*). Inputs are always
517 included in pairs. The former defines the type of input, the latter qualifies or quantifies
518 the input. This structure allows for adaptability of the code to various needs. Options
519 include the following:

520 – *what to do?*: 'toDo', followed by the desired analyses on of: 'FFT', 'PLOMB', 'pa-
521 rameters' or 'all' (default is 'all') - can be a cell array. This specifies what kind
522 of spatial analysis will be done on the input surface data. The spatial analysis is
523 calculated and averaged across every single profiles along the surface. The analyses
524 are the following:

- 525 * 'FFT', a power spectrum computed using a Fast Fourier Transform (FFT) al-
526 gorithm;
- 527 * 'PLOMB', a power spectrum computed using a least-squares Lomb-Scargle al-
528 gorithm;
- 529 * 'parameters', the calculation (as a function of scale) of the Root Mean Squared
530 (RMS), skewness, kurtosis and asymmetry averaged across all segments of a
531 given length on all profiles of the surface.

532 'all' simply performs all the analyses outlined above.

533 – *skip pre-processing?*: 'bypass', followed by 'zygo', 'pre-processing' or 'no' to be used
534 input is already in aligned clean grid form - input files are then (default is 'no').
535 'zygo' is specifically adapted to the proprietary data format of the white light in
536 Wong. 'pre-processing' simply skips any pre-processing. This option requires a
537 .mat structure with a field named 'grid' with the topography and a field name
538 'pointSpacing' specifying the point spacing (in meters). In either case the topography
539 must be aligned such that the positive x direction is the parallel direction.

540 – *for the parameter analysis, how many scales?* 'numberOfScales' followed by the
541 desired number of analysed scales. This option is relevant to the parameters analysis.
542 Note that this has a lot of effect on the amount of processing time (default is 10).

543 – *decimation*: 'decimationFactor' followed by the desired decimation factor (default is
544 1). Decimation is a useful tool to reduce computation time. The surface grid is sub-
545 sampled according to the decimation such that a decimation factor of k would imply
546 that only every k th point on the every k th will be considered for hte subsequent
547 analysis.

548 – *Instrument specific analysis* 'instrument' followed by 'white light', 'laser scanner' or
549 'lidar' (default does not set any instrument specific adjustments). Some instrument
550 specific pre-processing steps are taken. Please contact me if you intend to use this
551 as they may be highly dependent on the specific instrument used.

552 For instance, `surfaceprocessing('todo','FFT','bypass','zygo')` will only perform a power
553 spectral density analysis and will skip preprocessing and assume that all input will be in
554 the 'zygo' export .xyz format.

555 When the command is executed, the user will be prompted to navigate to the directory
556 where the input data is located. IMPORTANT: the directory must *only* contain files of
557 one data format. There cannot be other files or sub-directories in the directory. The user
558 will then be prompted to choose a destination for the output data. The requirements
559 for the output location are less stringent. However, it is advisable to choose an empty
560 directory such as to facilitate subsequent steps.

561 The next step is to visualize the output of the analysis. This is done using the *unpack*
562 *parameters* function. This function provides various visualization options for all files in
563 the directory chosen by the user. The first input (the *desired plot*) can be one of the
564 following:

- 565 '*FFT*': plot all power spectra;
- 566 '*PLOMB*': periodogram plot as determined by the Lomb-Scargle least squares anal-
567 ysis;
- 568 '*topostd*': plot of the root mean squared (RMS) as a function of scale;
- 569 '*topoSkew*': plot of skewness of height fields as a function of segment scale;
- 570 '*topoKurt*': plot of the the kurtoisis of height fields as a function of segment scale;
- 571 '*PowerVsDisp*': plot of power interpolated at a given scale as a function of displace-
572 ment;
- 573 '*RMSVsDisp*': model RMS at a given scale as a function of displacement
- 574 '*Grids*': shows both the original and pre-processed grid for the specified file 'file-
575 Name';
- 576 '*Best Fits*': best logarithmic fits to power spectra obtained from the fast fourier
577 transform analysis.

578 The functionality of the packages is broadly divided into three sections: 1) importing and
579 preprocessing data, 2) performing various spatial statistics on the pre-processed data, and
580 3) unpacking the analysis output into figures.

581 In order to run smoothly the all functions included in the package should be kept in the
582 same directory or on an accessible path.

583 For reference, here is a quick outline of what each function does:

- 584 *affine fit*: (from mathworks) Computes the plane of best fit using least squares
585 normal distance;
- 586 *align grid*: finds the smoothest directions in a grid using FFT spectra and rotates
587 and re-grids the input grid;
- 588 *fault spectral density simple*: Calculates the average lomb-scargle spectral density
589 every row of a N by M array;
- 590 *FindErr loop anisotropy*
- 591 *flatten XYZ*: removes planar trends from XYZ data by applying a rotations matrix
592 according to the best fit plane (*affine fit*);
- 593 *fractal model outlier*: Removes outlying segments according to a near-gaussian model
594 for the distribution of RMS values at specified segment lengths (or scales);

595 *frequency.spectrum*: Calculates the average lomb-scargle spectral density of all con-
596 tinuous segments on every single row of a N by M array;
597 *parse.zygo.format*: extracts the both the point spacing and topographic grid from
598 the exported zygo format. Can also remove planar trend from data (substracted
599 from grid);
600 *rotateZ*: applies rotation matrix on XYZ data
601 *surface.analysis*: Aggregates the analysis functions and applies them to an input
602 grid
603 *surface.cleaning*: removes outliers associated to surface defects
604 *surface.parameters*: calculates spatial statistics and parameters along segments as a
605 function of scale (RMS, skewness, directional asymmetry and kurtosis)
606 *surface.preprocessing.2*: deals with preprocessing input data (import data, cleaning
607 and gridding data)